

Short communication

On the use of the Radon Transform in studying nearshore wave dynamics



Rafael Almar ^{a,*}, Herve Michallet ^b, Rodrigo Cienfuegos ^{c,d}, Philippe Bonneton ^e,
Marion Tissier ^f, Gerben Ruessink ^f

^a UMR LEGOS (CNRS/CNES/IRD/Université de Toulouse), Toulouse, France

^b CNRS/UJF/G-INP, UMR LEGI, BP53, 38041, Grenoble, France

^c Departamento de Ingeniería Hidráulica y Ambiental, Escuela de Ingeniería, Pontificia Universidad Católica de Chile, Santiago, Chile

^d Centro Nacional de Investigación para la Gestión Integrada de Desastres Naturales (CIGIDEN-Conicyt/Fondap/15110017), Santiago, Chile

^e UMR EPOC (Université de Bordeaux/CNRS), Bordeaux, France

^f Department of Physical Geography, Faculty of Geosciences, Utrecht University, P.O. Box 80.115, 3508 TC Utrecht, The Netherlands

ARTICLE INFO

Article history:

Received 10 January 2014

Received in revised form 18 June 2014

Accepted 23 June 2014

Available online xxxx

Keywords:

Surf zone

Wave transformation

Wave propagation

Individual wave celerity

Wave reflection

Incoming and outgoing waves separation

ABSTRACT

In the nearshore, describing the complex individual wave dynamics remains a key challenge. In this paper we test the ability of the Radon Transform to produce estimates of individual wave celerities and to separate incoming and outgoing waves conserving the temporal characteristics. The Radon Transform is a projection of a two-dimensional field into polar space. Oblique features such as propagating crests in a spatio-temporal space are identified with density peaks in the polar space. In this paper, the Radon Transform is applied to synthetic test cases including a wide range of beach slopes and wave conditions. The Radon Transform shows good skills at estimating individual celerity and separating incoming and outgoing components with a relative RMS error lower than 10%, even a standing wave node. The accuracy is fairly insensitive to wave characteristics whereas the main limitations rise from the sampling scheme and are the number and density of wave gauges. The distance between gauges should be less than one third of the shortest wavelength, while the set of gauges should cover more than one third of the longest wavelength.

© 2014 Elsevier B.V. All rights reserved.

1. Introduction

The complexity of an incident short-wave (typically, 0.05–0.5 Hz) field increases while approaching the shore. For example, short waves induce long waves (~0.005–0.05 Hz) that reflect from the beach face, producing cross-shore patterns that may influence the height and celerity of individual short waves (Abdelrahman and Thornton, 1987; Roelvink and Stive, 1989). Limitations of techniques that aim to separate incoming and outgoing wave signals presently prevent an accurate description and understanding of wave-by-wave dynamics and interactions between short and long-wave fields. However, in the nearshore shallow water domain, the celerity of short waves is a key kinematic variable to describe energy fluxes and to derive bathymetric variations through the inversion of the dispersion relation (Catalán and Haller, 2008). While an average celerity can be estimated through cross-correlation techniques (Almar et al., 2008; Tissier et al., 2011), it becomes very inaccurate when applied to individual waves which often exhibit a substantial wave-to-wave celerity variability (i.e. dispersion from the mean value), in particular close to the breakpoint and in very shallow water (Catalán and Haller, 2008; Stive, 1984; Svendsen et al.,

2003; Tissier et al., 2013). Signal separation often relies on spectral approaches based on Fourier transformed wave time-series on a subarray of adjacent wave gauges (e.g. Battjes et al., 2004; Goda and Suzuki, 1976; Sheremet et al., 2002; van Dongeren et al., 2007). As pointed out by Baldock (2006), no rigorous separation procedure exists for irregular waves breaking over a sloping bed. Moving towards methods that estimate the amplitudes and phases of incident and reflected waves is required to perform wave-by-waves analysis and to obtain more insight into the complex wave interactions in the nearshore.

In this work, we aim to assess the ability of the Radon transform (RT, Deans, 1983; Radon, 1917) in describing nearshore wave dynamics from dense spatio-temporal data of sea surface elevation. The RT is commonly used in image processing and computer vision as edge detector, denoising, and line extraction (Murphy, 1986). In geosciences, applications exist in the field of seismology (de Hoop et al., 2008), ship waves (Copeland et al., 1995; Rey et al., 1990), regional ocean Rossby waves propagation (Cipollini et al., 1998). Its application to nearshore wave processes includes the tracking of the crests of individual waves (Yoo et al., 2011) and the detection of the swash front motion (Zhang et al., 2009).

In this paper we revisit the RT method in the context of coastal engineering applications focusing on nearshore wave dynamics. In Section 2 the theoretical aspects of the method are described briefly and the RT-based methods for retrieving incoming and outgoing waves and

* Corresponding author.

E-mail address: rafael.almar@ird.fr (R. Almar).

estimating individual wave celerity are presented. The influence of the sampling scheme is discussed. Realistic synthetic test cases are used to assess the method's accuracy, advantages and drawbacks in Section 3. Finally, we provide concluding remarks and guidelines for the application of the RT to coastal studies.

2. The Radon transform

2.1. Principle

The RT (Deans, 1983; Duda and Hart, 1972; Radon, 1917) $R(\rho, \theta)$ over a bidimensional field $\eta(x, y)$ can be defined as:

$$R(\rho, \theta) = \iint \eta(x, y) \delta(x \cos \theta + y \sin \theta - \rho) dx dy \quad (1)$$

where δ is the Dirac delta function, θ and ρ are the angle and distance from origin of the integration line defined as $\rho = x \cos \theta + y \sin \theta$. The origin is the center of the two-dimension field. Fig. 1 shows the application of the RT to a line defined as $y = -\frac{\cos \theta_o}{\sin \theta_o} x + \frac{\rho_o}{\sin \theta_o}$. In the Radon space, the signature of this line is an energy peak at (ρ_o, θ_o) . The RT is defined for all possible values of θ from $[0$ to $180^\circ]$ and ρ from 0 to the diagonal length of the field. For example the RT of a dx -dimension field is defined for ρ values between $[-\frac{\sqrt{2}}{2}d : +\frac{\sqrt{2}}{2}d]$.

The original field $\eta(x, y)$ can be back projected using the Inverse Radon Transform for all possible ρ and θ values as follow:

$$\eta(x, y) = \iint R(\rho, \theta) d\theta d\rho \quad (2)$$

The back projection can also be conducted for specified ranges of ρ and θ values.

2.2. Celerity of individual waves

In nearshore studies of cross-shore wave transformation based on dense one-dimensional array from shore-based remote sensing, wave gauges or numerical modeling, wave data are frequently represented in a spatio-temporal $x-t$ format, x being the cross-shore direction defined positive onshore. Each propagating wave appears as an oblique line in the $x-t$ space and has an associated peak in Radon space. Due to the integration process, the Radon transform is particularly suited for finding individual waves in a noisy or irregular wave field.

An illustration of the celerity estimation procedure through the RT is given in Fig. 2. Fig. 2a shows a realistic $x-t$ surface elevation wave field generated using a Boussinesq numerical model (Serr1D, Cienfuegos et al., 2010). Temporal and spatial resolutions respectively equal to $dt = 0.1$ s and $dx = 0.1$ m, dimension is 500×150 pts which represents a physical dimension of $50 \text{ s} \times 15 \text{ m}$. Irregular incoming waves (JONSWAP enhancement factor $\gamma = 3.3$, peak

period $T_p = 5$ s and significant wave height $H_s = 0.05$ m) are propagated over a constant $d = 0.5$ -m depth. Out of the domain shown in Fig. 2a, the reflection at the shore over a $1/20$ slope generates an outgoing component dominated by long waves. Incoming oblique short-crested wave trajectories are clearly visible. Each of these waves has a signature in the Radon space shown in Fig. 2b, materialized by a peak at (ρ, θ) . The width of the peak in the Radon space materializes the ability of the RT in determining the angle θ of the propagating feature; the narrower is this peak in angle space, the more accurate is the estimation. θ can be further converted into a wave celerity c (m/s) through the following transformation:

$$c = \tan(\theta) dx/dt \quad (3)$$

where dx and dt are the spatial and temporal resolution, respectively. Celerity in Fig. 2b shows some dispersion, with an average crests angle of $\theta = 68.3^\circ$ which gives $c = 2.51$ m/s using Eq. (3). In this definition, wave celerity is associated to the propagation of the crest, which is identified by a local maximum, and a positive peak in the Radon space. However, as shown in Fig. 2b, the RT can also be applied to the propagation of the wave trough which is identified as a negative peak in the Radon space. Here, the average troughs celerity is slightly smaller ($\theta = 66.9^\circ$, $c = 2.34$ m/s) to what found for crests, indicating a non-linear wave transformation.

Features that span across the entire $x-t$ field but show some large curvature like waves propagating in a variable water depth may not produce suitable peaks or trough in the polar space. To estimate wave celerity, a localized Radon Transform must be applied on a distance on which crest angle can be assumed constant, typically a distance shorter than a wavelength (Almar et al., 2008). This is done by reducing the $x-t$ field to a Wx -wide moving window where Wx is the number of points, or wave gauges, of the window.

2.3. Separation of incoming and outgoing waves

Contrary to the individual wave celerity estimation that needs a localized application of the RT, the separation of incoming and outgoing waves can be conducted over the whole $x-t$ wave field. If a wave field $\eta(x, t)$ contains both incoming and outgoing waves, the incoming and outgoing wave trains appear in the Radon space within the $\theta = [1^\circ - 89^\circ]$ and $\theta = [91^\circ - 179^\circ]$ intervals, respectively. The separation procedure is illustrated in Fig. 2. In Fig. 2b, the two groups of wave trains associated to incoming and outgoing waves can be clearly seen. These two groups are separated and reconstructed using the Inverse Radon Transform, applied separately at angles from 1 to 89° for incoming waves $\eta_{In}(x, t)$ (Eq. (4), Fig. 2c) and from 91° to 179° for outgoing waves $\eta_{Out}(x, t)$ (Eq. (5), Fig. 2d):

$$\eta_{In}(x, t) = \int_{-\infty}^{+\infty} \int_1^{89} R(\rho, \theta) d\theta d\rho \quad (4)$$

$$\eta_{Out}(x, t) = \int_{-\infty}^{+\infty} \int_{91}^{179} R(\rho, \theta) d\theta d\rho \quad (5)$$

2.4. Sensitivity analysis on the sampling scheme

The sampling scheme may be a limiting factor for the use of the RT in the description of wave characteristics, particularly when considering its application to field data. We address in this section the minimal number of wave gauges Wx and the distance between gauges dx required by the RT for obtaining a reasonable accuracy on the wave celerity and amplitude. In Fig. 3, the relative RMS error on the RT estimation of the incoming wave celerity Err_c and amplitude Err_A (resulting from incoming/outgoing decomposition) are evaluated for various sampling

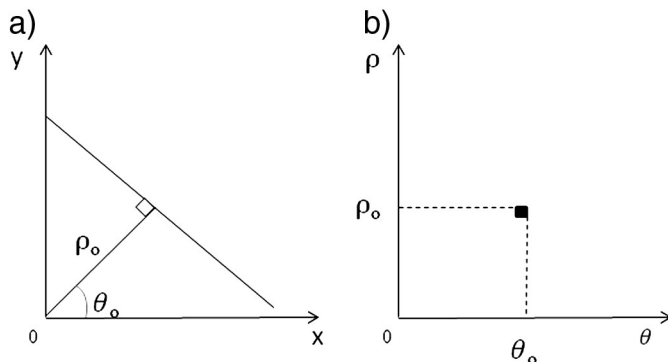


Fig. 1. Principle of the RT: a) a line defined by $y = -\frac{\cos \theta_o}{\sin \theta_o} x + \frac{\rho_o}{\sin \theta_o}$ and b) its signature as a peak at (ρ_o, θ_o) in Radon space.

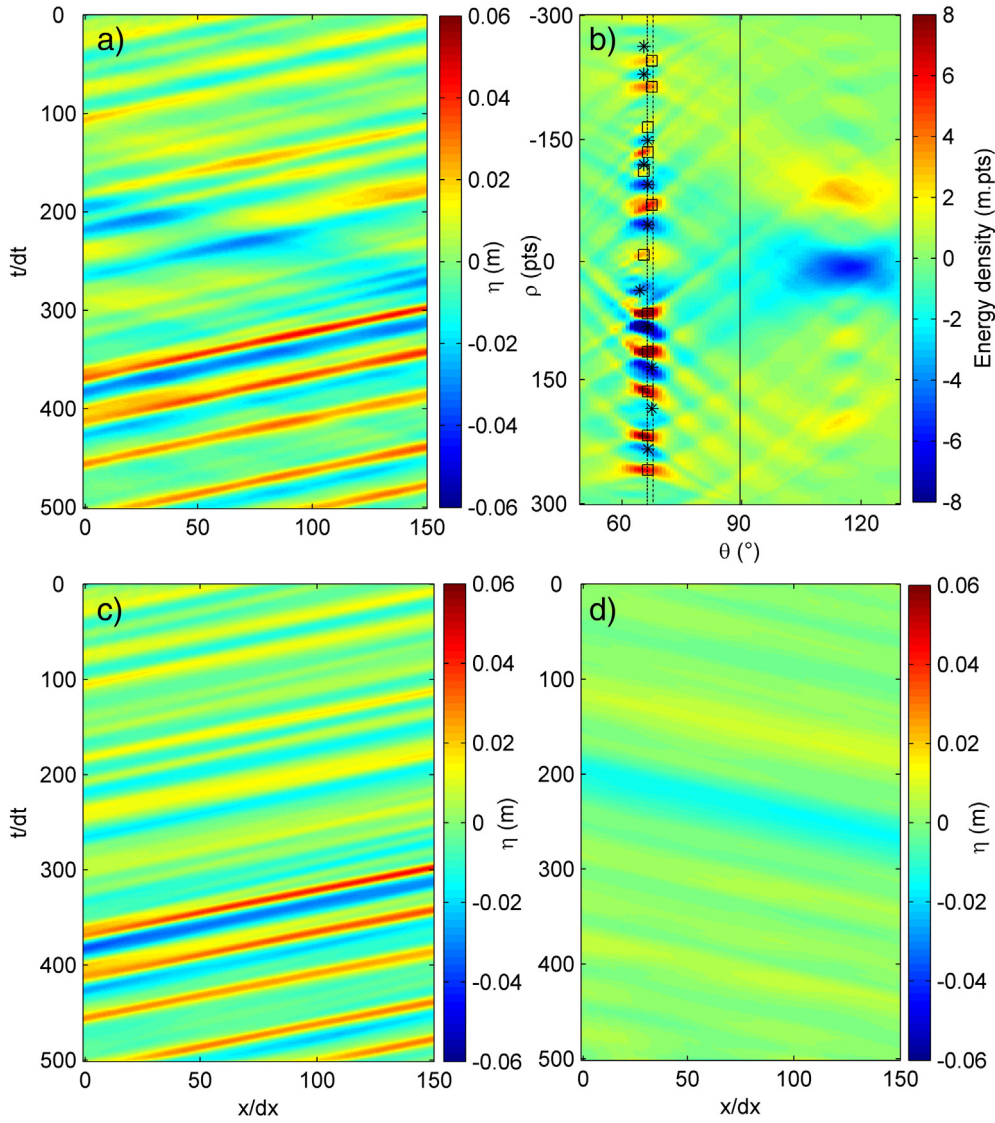


Fig. 2. Illustration on the use of the RT in estimating individual celerity and separating incoming from outgoing waves. a) x - t surface elevation wave field of irregular incoming short and outgoing long waves propagating over a constant $d = 0.5$ -m depth, b) associated Radon transform, with θ defined from the vertical t -axis. Local maxima and minima stand for individual crest (squares) and troughs (stars), respectively. Average angles of crests and troughs are represented as vertical dotted and dashed line, respectively. Solid line $\theta = 90^\circ$ marks the separation between incoming (1 to 89°) and outgoing motion (91 to 179°). c) Incoming and d) outgoing waves retrieved using Eqs. (4) and (5), respectively.

schemes of a single synthetic wave field. This x - t wave field is constituted of incoming monochromatic waves ($T = 5$ s, $A = 0.05$ m) propagated artificially (without using the Serr1D model) at the shallow water celerity $c = \sqrt{gd}$, over a $d = 1$ -m constant water depth, $g = 9.81$ m.s⁻² being the acceleration of gravity. Wx is varied such as $Wx/(L/dx)$ ranges from 0.05 to 2 and dx varying such as dx/L takes values from 0.01 to 0.8. A 0.1 threshold on the relative error is used for an accuracy considered as reasonable. Fig. 3a shows that the RT is limited by the number of wave gauges if the resolution is very high ($dx < L$): Err_A rapidly decreases with $Wx/(L/dx)$ and reaches values lower than 0.1 for $Wx/(L/dx) > 0.3$. The resolution can be a limitation as Err_A increases with dx/L and reaches values larger than 0.1 for $dx/L > 0.3$. For the RT estimation of the celerity, Fig. 3b shows that Err_c is only weakly sensitive to $Wx/(L/dx)$ for moderately high resolution $dx/L < 0.5$. Err_c remains also fairly non-sensitive to the resolution for $dx/L < 0.5$ but sharply increases to values larger than 1 for $dx/L > 0.5$. The domain of validity is larger for the celerity than for the amplitude estimation. This is due to the line-integration process of the RT that averages out signal when resolution weakens but does not affect the estimation of the phase and consequently the celerity.

These results have direct consequences on the estimation of the edge perturbation when applying the RT to a wave field. In line with results obtained for the influence of Wx and dx on the RT accuracy, the RT-derived wave characteristics can be used with confidence (at a 0.1 relative error level) at a minimal distance of $0.3 L$ from the on/offshore boundaries.

When using real datasets, the spatial resolution is not always regular and can substantially vary along the direction of wave propagation. In order to determine the impact of an irregular sampling, a random noise has been added to the previously used wave field, considering a sampling scheme in the RT validity domain (i.e. not limited by resolution or number of wave gauges). The spatial sampling irregularity is estimated through the dimensionless parameter $\sigma(dx)/(L \langle dx \rangle)$, where $\sigma(dx)$ and $\langle dx \rangle$ are the standard deviation and the average distance between gauges, respectively. The noise intensity is varied such as $\sigma(dx)/(L \langle dx \rangle)$ takes values from 0 to 0.14. Fig. 4 shows that Err_A increases steadily with growing irregularity but Err_c is rather not sensitive and remains lower than the 0.1 threshold. Err_A reaches the 0.1 threshold when the dispersion is about 10% of the wavelength. This result is in line with what found for the impact of increasing dx on Err_A and Err_c : when irregularity increases, the RT-integration process tends to average-out the signal amplitude

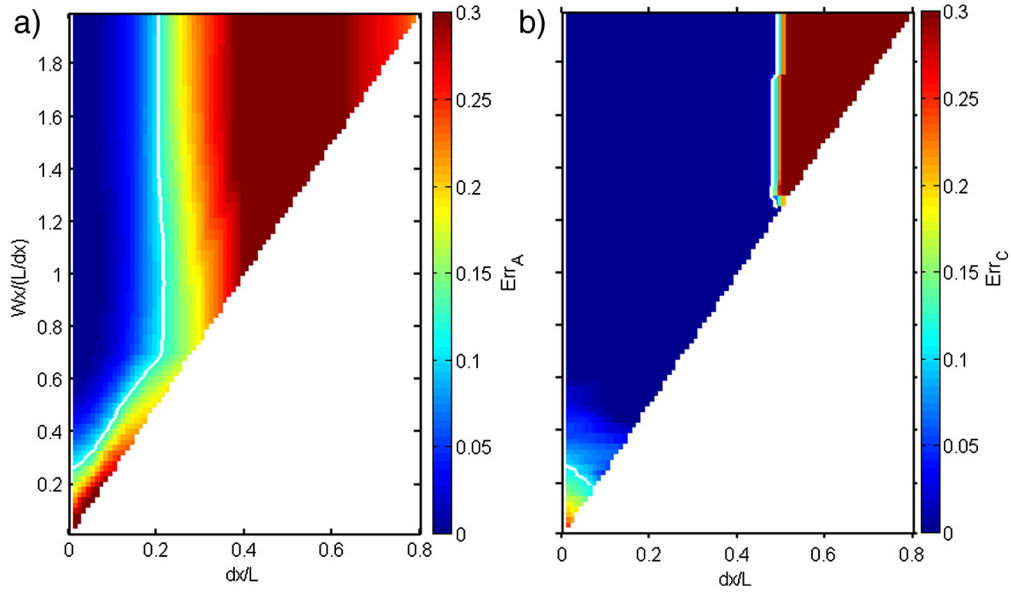


Fig. 3. Sensitivity of the RT accuracy with the number of wave gauges $W_x/(L/dx)$ and dimensionless resolution dx/L on the estimation of wave a) amplitude and b) celerity. The white thick line stands for the method's accuracy acceptable threshold defined as a RMS relative error of 0.1.

whereas the signal phase and consequently the celerity estimation is less affected.

3. Applications

3.1. Realistic synthetic test cases

The RT was applied to laboratory datasets in Almar et al. (2012, 2013) and showed good skills but the validation of the method was not possible since this requires controlled synthetic data. Here, to validate and test the RT over a wide range of waves and beach conditions, various numerical test cases have been generated using a Boussinesq numerical model (Serr1D, Cienfuegos et al., 2010; see Table 1) that has been extensively validated for both short- and long-wave propagation. Beach reflection is set to zero to control outgoing signals. This is done in the model by increasing the friction to a very large value close

to the shore. The sampling is $dx = 0.25$ m in space and $dt = 0.1$ s in time over 90 s (900 pts). Spatial dimension depends on beach slope. Test cases are separated into 3 series; monochromatic (A), bichromatic (B) and irregular JONSWAP (C) waves. Sub-series stand for sensitivity analyses on wave and beach parameters. The aim of series A was to perform sensitivity analyses on various beaches (slope, water depth) and wave conditions (incoming and outgoing). Series B aimed at testing the skill of the RT in presence of long waves. Series C aimed at testing the RT for a realistic case, particularly in the occurrence of wave-to-wave interactions (e.g. celerity dispersion, merging). The outgoing signal was generated artificially by taking incoming timeseries at a location close to the shore (500 pts) and propagated offshore at shallow water celerity. A sinusoidal signal was used for the A series. For B and C series,

Table 1

Characteristics of the synthetic RT test cases. sl stands for beach slope, A for incoming wave amplitudes, H_s for significant wave height and T_p for peak period (JONSWAP cases), d_0 for outer point water depth, and γ for the JONSWAP enhancement factor. Subscripts *inc* and *out* stand for incoming and outgoing components.

Test cases	Waves	Beach
Sampling: $dx = 0.25$ m, $dt = 0.1$ s, 900 pts in time (90 s), spatial dimension depends on slope.		
Serie A - Monochromatic		
A1 (varying d_0)	$A = 0.02$ m, $T = 5$ s No beach reflection	$d_0 = 0.5, 1, 3$ m
A2 (varying sl)	$A = 0.02$ m, $T = 5$ s No beach reflection	$d_0 = 1$ m, $sl = 1/40, 1/80, 1/100$
A3	$A_{inc} = 0.02$ m, $T_{inc} = 5$ s, $A_{out} = 0.01$ m, $T_{out} = 10$ s Beach reflection	$d_0 = 1$ m, $sl = 1/80$
Serie B - Bichromatic		
B1	$A1 = 0.09$ m, $T1 = 5$ s, $A2 = 0.04$, $T2 = 5.5$ s No beach reflection	$d_0 = 1$ m, $sl = 1/80$
B2	$A1 = 0.09$ m, $T1 = 5$ s, $A2 = 0.04$, $T2 = 5.5$ s Beach reflection	$d_0 = 1$ m, $sl = 1/80$
Serie C-Irregular		
C1	$\gamma = 3.3$, $T_p = 5$ s, $H_s = 0.2$ m No beach reflection	$d_0 = 1$ m, $sl = 1/80$
C2	$\gamma = 3.3$, $T_p = 5$ s, $H_s = 0.2$ m Beach reflection	$d_0 = 1$ m, $sl = 1/80$
C3	$\gamma = 3.3$, $T_p = 20$ s, $H_s = 0.02$ m Beach reflection	$d_0 = 1$ m, $sl = 1/80$

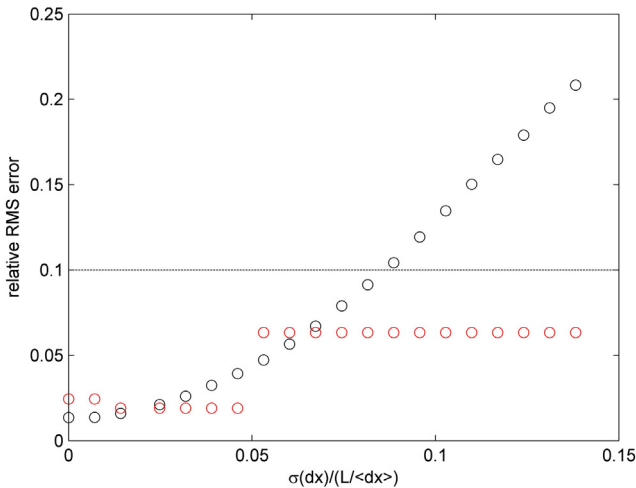


Fig. 4. Sensitivity of the RT accuracy with the dimensionless spatial sampling irregularity $\sigma(dx)/(L\langle dx \rangle)$, where $\sigma(dx)$ and $\langle dx \rangle$ are the standard deviation and the average distance between gauges, respectively. Black and red circles are the RMS relative error on RT-estimated amplitude Err_A , and celerity Err_C , respectively. The black dashed line stands for the method's accuracy acceptable threshold of 0.1. (For interpretation of the references to colour in this figure legend, the reader is referred to the web version of this article.)

the low-frequency component (low-pass filtered signal with a cut-off frequency of 3/5 of peak frequency) of the incoming signal extracted at a location close to the beach was used. In Sections 3.2 and 3.3 the skill of the RT is tested using these test cases.

3.2. Individual wave celerity

Individual celerity is estimated using the procedure detailed in Section 2.2 over an arbitrary $Wx = 50$ -pts wide moving window that reaches validity criteria defined in Section 2.4. The validation is conducted with celerities obtained from the tracking of individual crest elevation maxima while waves propagate to the shore (see Fig. 5, upper panels). In Fig. 5, the skill of the RT in estimating wave celerity is tested for varying water depth (A1), beach slope (A2), bichromatic (B1) and irregular (C1) cases. For these 4 cases, the relative RMS difference between RT-estimated celerity (c_{RT}) and crest-tracking (c_t) celerities, is lower than 4%. However, the RT tends to underestimate celerity for larger celerity values. This behavior appears in the regression coefficient between individual celerities, which is lower than one (0.97, $R^2 = 0.98$, statistically significant at the 0.05 level). This slight underestimation is

due to the choice of a fixed spatial window, which is a limitation when the wavelength increases, as found in Section 2.4. The B1 and C1 cases show substantial celerity dispersion due to the presence of underlying long waves. This dispersion, computed as the standard deviation, is illustrated in Fig. 5g and 5h as error bars which indicate a good agreement between RT-estimated and crest-tracking methods. More details can be found in Fig. 5o and 5p which show timeseries of celerity at a given location, close to the beach ($x/dx = 500$ pts). These results indicate that the RT well estimates the individual celerities and is thus able to catch the modulation of celerity due to long waves and wave-to-wave interactions.

3.3. Separation of incoming and outgoing waves

The separation procedure described in Section 2.3 is applied here to various test cases detailed in Table 1. The first 3 columns in Fig. 6 show the application of the RT to monochromatic (A3), bichromatic (B2) and random (C2) cases where outgoing long waves are superimposed on incoming waves. In the fourth column, the RT is also tested for the quasi-standing wave case C3 which is extremely challenging for the

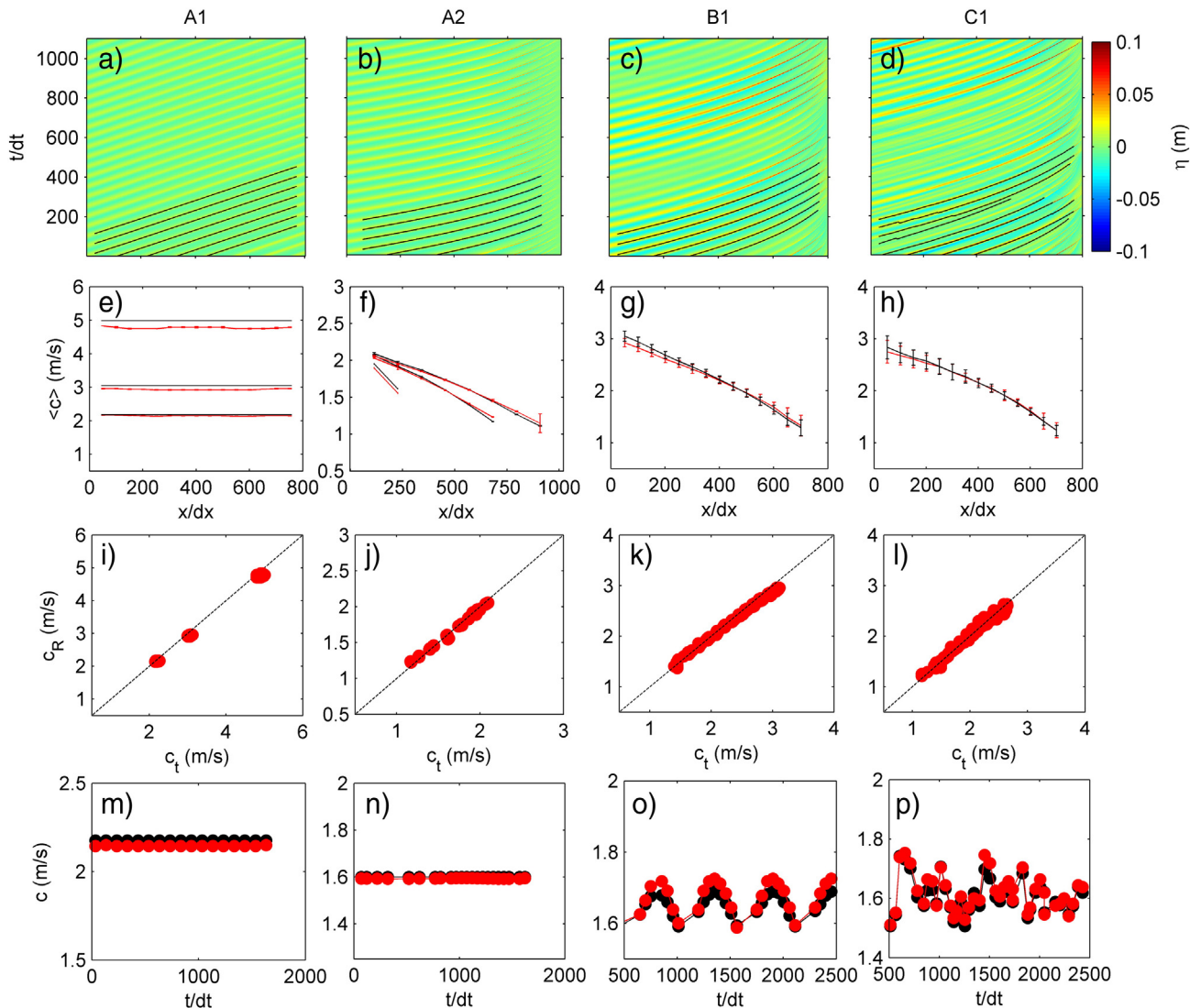


Fig. 5. RT celerity estimation for A1, A2, B1, C1 test cases (see Table 1). a–d) spatio-temporal surface elevation, η (m), together with examples of tracked crest trajectories (black lines), e–h) average celerity $\langle c \rangle$ and standard deviation (as error bar) from crest tracking (in red) and RT (in black), i–l) individual RT-derived celerity (c_R) versus tracking-derived celerity (c_t) with the 1:1 line (black dashed line), and m–p) timeseries of individual celerity at $x/dx = 500$. In e) and i) are represented the 3 cases of series A1 with water depth of 0.5, 1 and 3 m, while only the $d = 1$ -m case is plotted in a). In f) and j) are represented the 3 cases of A2 with beach slopes of 1/40, 1/80 and 1/100 while only the 1/80 case is plotted in b). (For interpretation of the references to colour in this figure legend, the reader is referred to the web version of this article.)

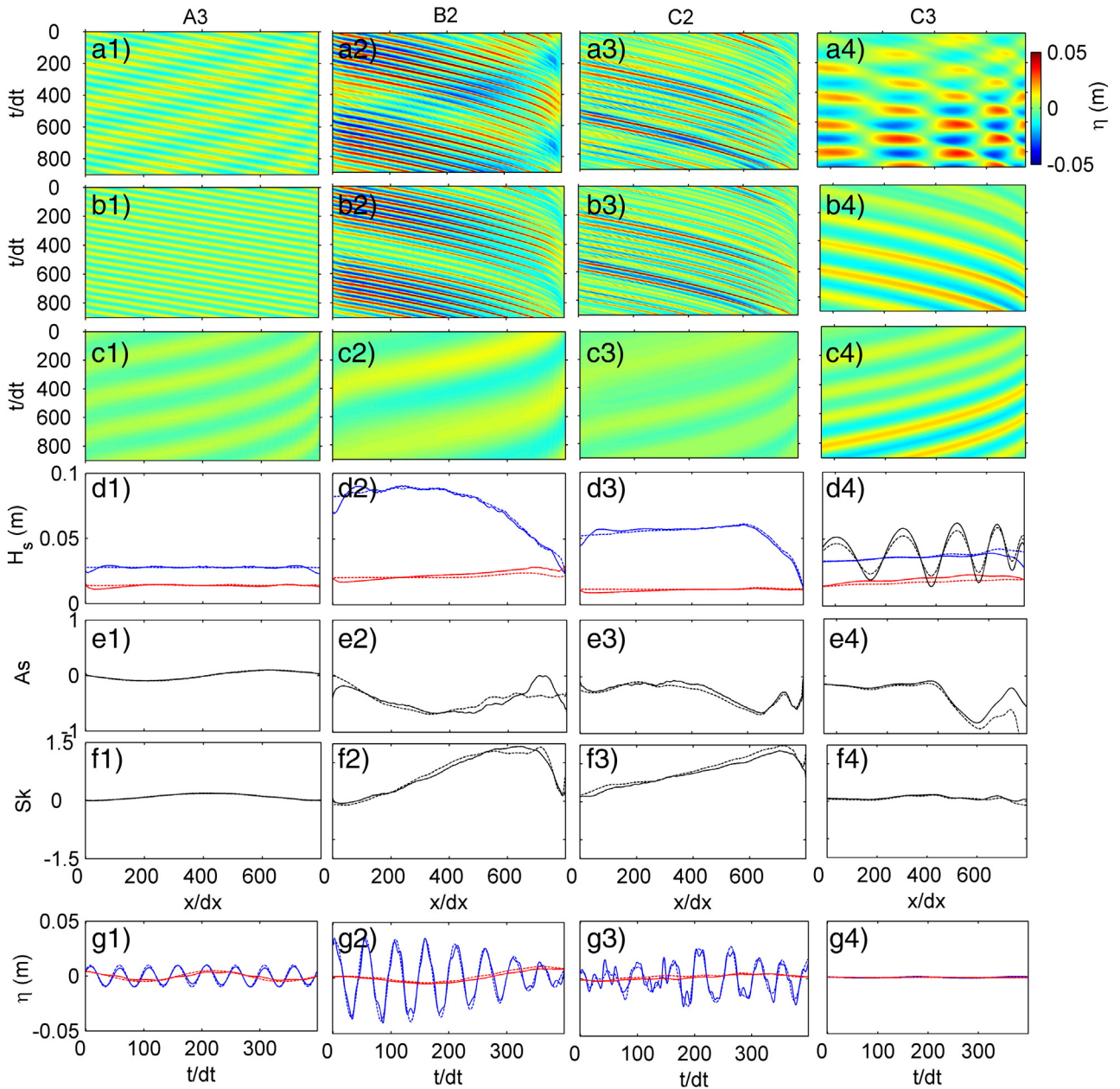


Fig. 6. RT separation of incoming and outgoing waves for the A3, B2, C2 and C3 test cases. From top to bottom: a1–4) total, b1–4) incoming and c1–4) outgoing waves, d1–4) wave height H_s (incoming in blue and outgoing in red, total in black in d4)) along x , e1–4) asymmetry and f1–4) skewness of incoming waves, and g1–4) timeseries of surface elevation (incoming in blue and outgoing in red) at $x/dx = 500$ pts. Solid and dashed lines are RT-derived and original components, respectively. (For interpretation of the references to colour in this figure legend, the reader is referred to the web version of this article.)

separation methods because wave signature decays at nodes. For the first 3 cases (A3, B2, C2), the mean relative RMS error on wave height is 4 % and 6 % for incoming and outgoing waves, respectively (Fig. 6d (1–3)). The absence of a clear difference between the method skills between the three cases underlines the weak dependence of the RT performances to wave characteristics for such dense datasets. As seen in Fig. 6d (1–3), large errors are observed at distances shorter than $L/3$ from the on/offshore boundaries where the RT does not have enough signal to determine properly wave characteristics, as previously described in Section 2.4. For the C3 long wave case (fourth column in Fig. 6), the average accuracy slightly worsen while compared to other cases, showing errors of 6 and 11 % for incoming and outgoing wave height, respectively. The reasonable result of the RT for such quasi-standing C3 case is made possible by the line-integration procedure

that allows a good estimate of incoming and outgoing waves, even at standing wave nodes (Fig. 6d4). Noteworthy, an analyze (not shown) indicates that the RT-separation performance is not sensitive to the difference of period between incoming and outgoing waves.

One of the strengths of the RT is the conservation of temporal characteristics of the signal. The latter is investigated specifically through the estimation of incoming wave asymmetry and skewness (Fig. 6e (1–4) and 6.f (1–4)) which provide information on the vertical and horizontal asymmetry, respectively. Overall, the RT well catches the steady increase of skewness and variations of asymmetry along the profile, which is a clear indicator of the good skills of the RT to reproduce wave shape changes. As a complement, timeseries of surface elevation for outgoing and incoming waves are shown in Fig. 6g (1–4), taken in the shoaling zone at $x/dx = 500$ pts. A good agreement is found between

the RT and original elevations. Both incoming and outgoing wave phases are well captured. This underlines that the RT conserves temporal characteristics and can be used for wave-by-wave analyses.

4. Conclusions

The possibilities offered by the Radon Transform in describing near-shore wave dynamics from synthetic datasets have been investigated. The Radon Transform is based on a polar projection which is well suited to spatio-temporal wave data format and conserves temporal characteristics of waves. The skills of the Radon Transform were tested over realistic test cases generated using a Boussinesq model: monochromatic, bichromatic and irregular waves. The Radon Transform is capable of quantifying individual wave celerity and separating incoming and outgoing waves. The mean relative RMS error for these test cases is lower than 10% for both the separation of incoming and outgoing waves and the estimation of individual celerity. The line-integration procedure of the Radon Transform is one of the main advantages of the method because it reduces noise associated to individual wave celerity estimation and allows separating incoming from outgoing waves even at nodes of standing waves but represents in return a drawback for non-continuous or rapidly varying wave signal.

This paper also provides guidelines for RT users, from a sensitivity analysis conducted on the sampling scheme. Results show that the minimal number of wave gauges has to cover at least 1/3 of the wavelength and the distance between sensors has to be smaller than 1/3 of the wavelength. Accuracy on wave amplitude estimation decreases with increasing irregularity whereas celerity estimation is less sensitive. Overall, wave celerity and separation between incoming and outgoing waves can be obtained with an accuracy better than 10%, at least at 1/3 wavelength from the edges, for a typical resolution of such as $dt < < T$ and $dx < L/3$. From its characteristics, it is expected that the application of the RT will bring new insight in nearshore wave dynamics, in particular while moving toward an individual wave approach.

Acknowledgments

This work has been supported by French INSU LEFE/EC2CO programs, FONDECYT research grant N°11060312 and by the European Community's Seventh Framework Program through the grant to the budget of the Integrated Infrastructure Initiative Hydralab IV, Contract no. 261520. RC funded by Fondecyt research grant No.1120878 and Conicyt/Fondap/15110017.

References

Abdelrahman, S.M., Thornton, E.B., 1987. Changes in the short wave amplitude and wave-number due to the presence of infragravity waves. Proceedings of the Speciality Conference on Coastal Hydraulics. American Society of Civil Engineers, New York, pp. 458–478.

Almar, R., Bonneton, P., Senechal, N., Roelvink, D., 2008. Wave celerity from video imaging: a new method. Proc. Int. Conf. Coastal Eng. 1 (5), 661–673.

Almar, R., Cienfuegos, R., Gonzalez, E., Catalan, P.A., Michallet, H., Bonneton, P., Castelle, B., Suarez, L., 2012. Barred beach morphological control on infragravity motion. ICCE, Santander, Spain.

Almar, R., Bonneton, P., Michallet, H., Cienfuegos, R., Ruessink, G., Tissier, M., 2013. On the use of the radon transform in studying wave dynamics: application to GLOBEX laboratory data. Proc. Coastal Dynamics 2013.

Baldock, T.E., 2006. Long wave generation by the shoaling and breaking of transient wave groups on a beach. Proc. R. Soc. London, Ser. A 462, 1853–1876.

Battjes, J.A., Bakkenes, H.J., Janssen, T.T., Van Dongeren, A.R., 2004. Shoaling of subharmonic gravity waves. J. Geophys. Res. (ISSN: 0148-0227) 109. <http://dx.doi.org/10.1029/2003JC001863>.

Catalán, P.A., Haller, M.C., 2008. Remote sensing of breaking wave phase speeds with application to non-linear depth inversions. Coast. Eng. 55 (1), 93–111.

Cienfuegos, R., Barthélemy, E., Bonneton, P., 2010. A wave-breaking model for Boussinesq-type equations including roller effects in the mass conservation equation. J. Waterw. Port Coast. Ocean Eng. 136, 10–26.

Cipollini, P., Cromwell, D., Quartly, G.D., 1998. Observations of Rossby waves propagation in the Northeast Atlantic with TOPEX/POSEIDON altimetry. Adv. Space Res. 22 (11), 1553–1556.

Copeland, A.C., Ravichandran, G., Trivedi, M.M., 1995. Localized radon transform-based detection of ship wakes in sar images. IEEE Trans. Geosci. Remote Sens. 33, 35–45.

De Hoop, M., Smith, H., Uhlmann, G., Van der Hilst, R., 2008. Seismic imaging with the generalized Radon transform: A curvelet transform perspective. Inverse Prob. 25, 025005.

Deans, S., 1983. The Radon transform and some of its applications, 1st edition. John Wiley & Sons, New York (289 pp., ISBN 13: 9780471898047).

Duda, R.O., Hart, P.E., 1972. Use of the Hough Transformation to Detect Lines and Curves in Pictures. Commun. ACM 15, 11–15.

Goda, Y., Suzuki, Y., 1976. Estimation of incident and reflected waves in random wave experiments. Proceedings of 15th International Conference on Coastal Engineering. ASCE, Honolulu, HI, pp. 828–845.

Murphy, L.M., 1986. Linear feature detection and enhancement in noisy images via the Radon transform. Pattern Recogn. Lett. 4, 279–284.

Radon, J., 1917. Über die Bestimmung von Funktionen durch ihre Integralwerte längs gewisser Mannigfaltigkeiten. Berichte Sächsische Akademie der Wissenschaften, Leipzig. Math.-Phys. Kl. 69, 262–267.

Rey, M.T., Tunaley, J.K., Folinsbee, J.T., Jahans, P.A., Dixon, J.A., Vant, M.R., 1990. Application of Radon transform techniques to wake detection in Seasat-A SAR images. IEEE Trans. Geosci. Remote Sens. 28, 553–560.

Roelvink, J.A., Stive, M.J.F., 1989. Bar-generating cross-shore flow mechanisms on a beach. J. Geophys. Res. 94, 4785–4800.

Sheremet, A., Guza, R.T., Elgar, S., Herbers, T.H.C., 2002. Observations of nearshore infragravity waves: Seaward and shoreward propagating components. J. Geophys. Res. 107 (C8), 3095. <http://dx.doi.org/10.1029/2001JC000970>.

Stive, M.J.F., 1984. Energy dissipation in waves breaking on gentle slopes. Coast. Eng. 8, 99–127.

Svendsen, I.A., Qin, W., Ebersole, B.A., 2003. Modeling waves and currents at the LSTF and other laboratory facilities. Coast. Eng. 50, 19–45.

Tissier, M., Bonneton, P., Almar, R., Castelle, B., Bonneton, N., Nahon, A., 2011. Field measurements and non-linear prediction of waves celerity in the surf zone. Eur. J. Mech. B. Fluids 30, 635–641.

Tissier, M., Almar, R., Bonneton, P., Michallet, H., de Bakker, A., Ruessink, B.G., 2013. Role of Short and Long-Wave interaction on wave celerity in the Surf zone of a low-sloping beach. Proceeding of Coastal Dynamics 2013, June 2013, Arcachon, France.

van Dongeren, A.R., Battjes, J.A., Janssen, T.T., van Noorloos, J., Steenbergen, K., Reniers, A., 2007. Shoaling and shoreline dissipation of low-frequency waves. J. Geophys. Res. 112 (C02011). <http://dx.doi.org/10.1029/2006JC003701>.

Yoo, J., Fritz, H., Haas, K., Work, P., Barnes, C., 2011. Depth inversion in the surf zone with inclusion of waves non-linearity using video-derived celerity. J. Waterw. Port Coast. Ocean Eng. 137 (2), 95–106.

Zhang, S., Zhang, C., Qi, Z., 2009. Waves swash velocity estimation using ridgelet transform. 9th Int. Conf. Electronic Meas. & Instr. ICEMI 09, pp. 1078–1081.